Lab on a Chip

PAPER

View Article Online
View Journal

Cite this: DOI: 10.1039/d6lc00197a

A microfluidic approach to evaluating surface protection from nonspecific antibody adsorption

Yulia Tobolovskaya, [a] Bexi M. Bustillo-Perez,[a] Yingshan Ma, [a] Nadine Löw,[b] Ophélie Zeyons,[b] Daniel A. Richards [c] and Eugenia Kumacheva *[adef]

Received 1st March 2026,
Accepted 1st May 2026

DOI: 10.1039/d6lc00197a

rsc.li/loc

Nonspecific antibody adsorption to solid surfaces remains a challenge in the development and use of formulations for immunotherapies, as it can compromise antibody structure and therapeutic function. Here, we introduce a photoluminescent carbon dot (C-dot) nanointerface integrated within a microfluidic platform for real-time, quantitative evaluation of antibody adsorption and surface protection strategies. Surface-immobilized C-dots exhibited photoluminescence quenching due to interactions with antibodies, thereby reporting on real-time adsorption to the surface of the microfluidic device. The approach combines tailored C-dot synthesis and their covalent immobilization onto the microchannel surface, while fluorescence microscopy enables continuous monitoring of antibody adsorption under flow. Using this approach, we evaluated the performance of surface-protecting surfactant molecules. The platform provided reproducible, concentration-resolved measurements across therapeutically relevant antibody concentrations. This strategy offers a time- and material-efficient route for screening anti-fouling agents, guiding the rational design of antibody-compatible surfaces. More broadly, the use of the C-dot nanointerface integrated with microfluidics establishes a versatile strategy for studying protein–surface interactions for immunosensing applications.

Introduction

Antibody engineering is a wide-reaching field that impacts different industries, but most notably, healthcare and diagnostics.[1,2] Antibodies and antibody–drug conjugates are an emerging class of biotherapeutics used for the systemic treatment of cancers, infections, autoimmune and Alzheimer's conditions.[3–6] The predominant antibody format approved by the US Food and Drug Administration (FDA) and the European Medicines Agency (EMA) is immunoglobulin G (IgG), which is abundantly found in human and animal serum.[7,8]

Therapeutic antibodies are frequently formulated at high concentrations (>100 mg mL^{-1}), allowing clinically relevant doses to be delivered *via* subcutaneous injection within limited volumes (typically ≤1–2 mL).[9–14] The intrinsically amphiphilic nature of antibodies renders them prone to non-specific adsorption to different surfaces.[15–17] Adsorption causes antibody loss during manufacturing, transportation, and storage.[13,16,18] In addition, changes in antibody conformation upon adsorption and desorption affects their functionality. These challenges have stimulated the development of surface-protective agents—most notably, non-ionic amphiphilic molecules (surfactants) attaching to hydrophobic surfaces with their hydrophobic fragment, while their hydrophilic moiety extends into an aqueous solution, creating a steric barrier that reduces antibody attachment to the surface.[12,19,20] These molecules compete with antibodies for adsorption sites, thereby forming a protective surface layer suppressing antibody adsorption and enhancing the stability and shelf-life of therapeutic antibody formulations.[20–22] For example, they have been used to prevent the adsorption of polyclonal bovine IgG on borosilicate glass and polydimethylsiloxane (PDMS), two materials widely employed in antibody research, storage and administration.[18,22,23]

The discovery and optimization of effective anti-biofouling compounds require the implementation of quantitative analytical methods to study antibody adsorption to solid surfaces. Currently used methods include surface plasmon resonance (SPR), ellipsometry, quartz crystal microbalance with dissipation monitoring (QCM-D), neutron reflectometry,

[a] Department of Chemistry, University of Toronto, 80 Saint George street, Toronto, ON, Canada. E-mail: eugenia.kumacheva@utoronto.ca
[b] BASF SE, Carl-Bosch-Straße 38, D-67056 Ludwigshafen, Germany
[c] Department of Chemistry and Applied Biosciences, ETH Zürich, Vladimir-Prelog-Weg 1, 8049 Zürich, Switzerland
[d] Department of Materials Science and Engineering, University of Toronto, 184 College St, Toronto, ON, M5S 3E4, Canada
[e] Department of Chemical Engineering and Applied Chemistry, University of Toronto, 200 College St, Toronto, ON, M5S 3E5, Canada
[f] Institute of Biomedical Engineering, University of Toronto, 164 College St, Toronto, ON, M5S 3G9, Canada

and single-molecule microscopy.[21,24–28] These methods have at least one of the following limitations. They either lack high-throughput and real-time screening capabilities, or have insufficient sensitivity, or need a large amount of antibodies and cost-intensive reagents. The development of a high-throughput and cost-effective methodology for real-time monitoring of antibody–surface interactions would enable the rapid screening, decision-making and optimization of next-generation anti-fouling agents.

To address these limitations, we developed a fluorescence assay-based microfluidic (MF) platform for the real-time studies of antibody adsorption to solid surfaces. Our approach utilizes quenching of the photoluminescence (PL) of a fluorophore reporter (carbon dots, C-dots) immobilized on the surface of the MF device following adsorption of polyclonal bovine IgG antibodies (pAbs) from the solution perfused through a microchannel.[29–31] The reduction in the degree of PL quenching of C-dots in the presence of an antifouling agent was used as the indication of the surface protection from the pAbs adsorption. For the case study, we used a block copolymer of poly(ethylene oxide) and poly(propylene oxide) (Kolliphor® P 188 Bio), and a polymeric surfactant composed of poly(ethylene oxide) chains attached to a sorbitan monolaurate backbone (Kolliphor® PS 20). The trends observed for the antifouling properties of surface-protective agents using an MF platform were validated using the QCM-D method and the Bradford assay. The utilization of the fluorescence assay-based MF platform is a promising strategy for screening antifouling properties of surface-protective agents.

Results and discussion

Fig. 1 outlines the approach to studies of pAbs adsorption in the MF platform. Following the synthesis of C-dots, they are covalently attached to the surface of PDMS microchannels (Fig. 1A). The PL intensity of the surface-bound C-dots is examined using fluorescence microscopy. During perfusion of the solution of pAbs through the MF channel, they adsorb onto the C-dots and the non-functionalized PDMS surface (Fig. 1B). We hypothesized that interactions between C-dots and pAbs would lead to the change of either PL emission wavelength or PL intensity, and real-time monitoring of these changes using fluorescence microscopy could serve as a measure of pAbs adsorption to the PDMS surface. Following these experiments, the surface of PDMS was coated with a surface-protecting surfactant, and the pAbs solution was perfused through the microchannel (Fig. 1C). A reduced change in PL properties of C-dots, in comparison with the unprotected C-dot coated surface, would serve as a measure of antifouling performance.

In the present work, C-dots were selected as the fluorophore reporters owing to their biocompatibility, colloidal stability in water, high quantum yield, controllable PL emission wavelength,[29–32] and binding to organic molecules.[31,33,34] We synthesized C-dots by the solvothermal synthesis.[29,35,36] The representative transmission electron microscopy (TEM) image in Fig. 2A reveals that C-dots had a close-to-spherical shape and an average diameter of 4.4 ± 1.7 nm (Fig. S1A, SI). The PL emission spectra of C-dots were acquired at an excitation wavelength, λ_{ex}, of 344 nm, at which the C-dots displayed a strong emission band centered at 435 nm (Fig. 2B). The PL intensity increased linearly with C-dot concentration in an aqueous solution from 0.1 to 0.5 mg mL^{-1} (Fig. S1B, SI), while the emission wavelength remained unchanged (Fig. S1C, SI). The PL properties of C-dots in solution were stable at room temperature over one week (Fig. S1D and E, SI). Based on the results of X-ray photoelectron spectroscopy (XPS) analysis, the survey spectrum displayed dominant peaks corresponding to C 1s, N 1s, and O 1s of the

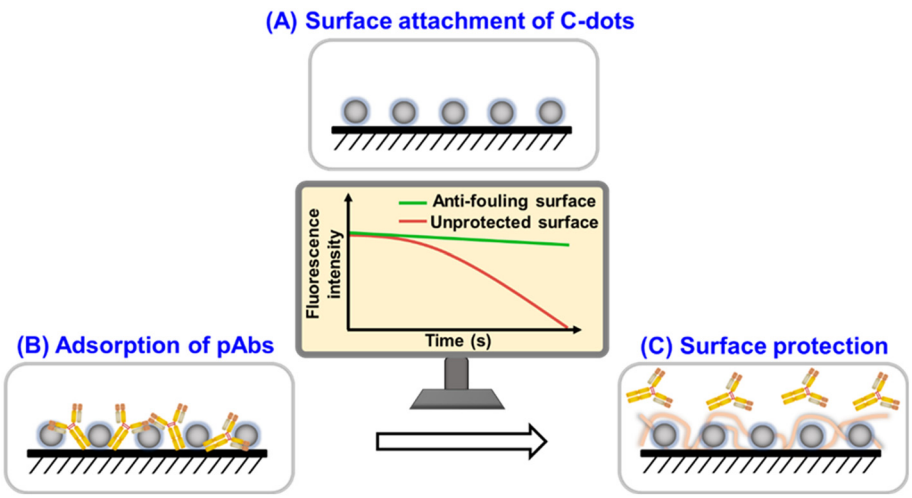

Fig. 1 Illustration of the approach to studies of real-time adsorption of pAbs to solid surfaces. (A) Attachment of C-dots acting as a fluorescent reporter to the surface. (B) Adsorption of pAbs to the surface carrying C-dots. (C) Surface protection from adsorption of pAbs by the antifouling surfactant. Fluorescence microscopy is used to monitor fluorescence of C-dots directly interacting with pAbs and C-dots interacting with pAbs in the presence of the surface-protecting surfactant.

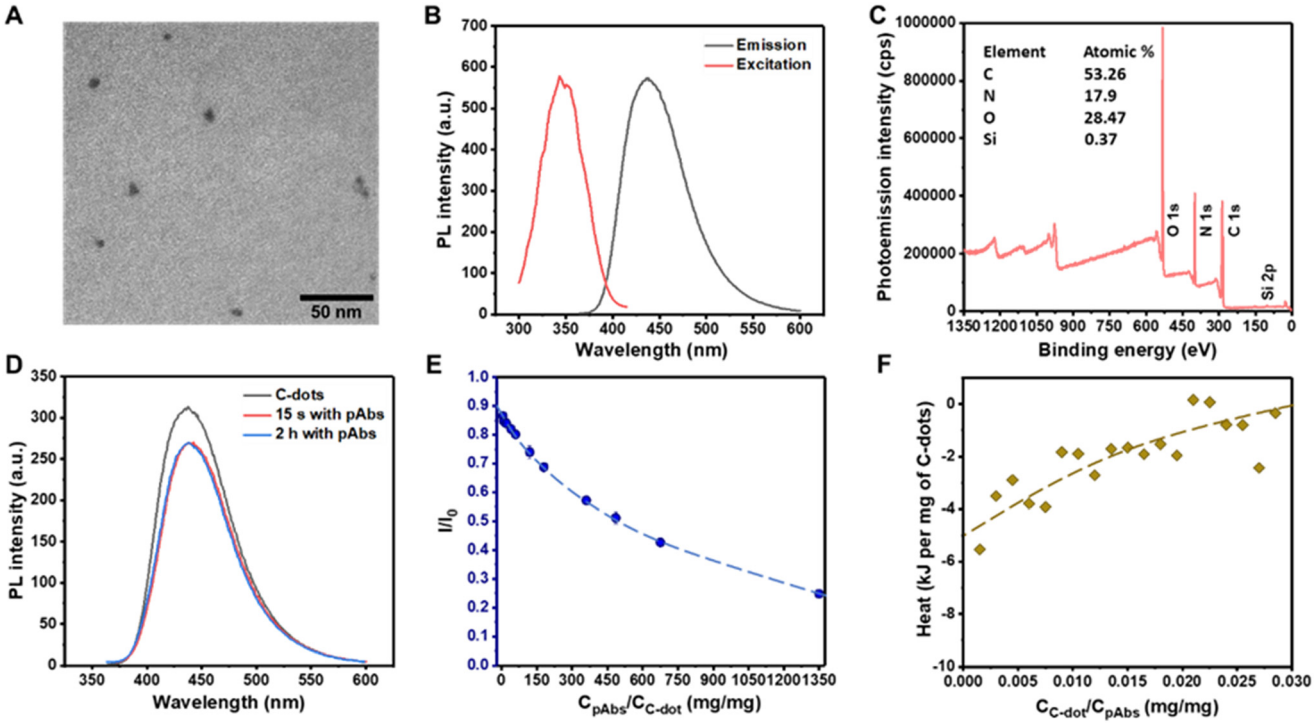

Fig. 2 Characterization of C-dots and their interactions with pAbs. (A) TEM image of C-dots. (B) Fluorescence excitation and emission spectra of 0.5 mg mL^{-1} C-dots in solution at 344 nm excitation. (C) XPS survey spectrum of 50 mg mL^{-1} C-dots in solution drop-casted onto a silicon wafer and dried. (D) Fluorescence emission spectra of 0.25 mg mL^{-1} C-dots during incubation with 15 mg mL^{-1} pAbs in 1 mL histidine buffer ($C_{C\text{-dot}}/C_{pAbs}$ = 60 mg mg^{-1}). (E) Variation in the I/I_0 as a function of $C_{pAbs}/C_{C\text{-dot}}$. Standard deviations of I/I_0 were obtained from three independent repeats. (F) ITC profile for the titration of C-dots into a solution of pAbs, reporting changes in heat as a function of $C_{C\text{-dot}}/C_{pAbs}$. The dashed lines are provided for eye guidance.

C-dots, with a trace Si 2p signal at 101.4 eV (0.37 at%) attributed to the underlying silicon substrate (Fig. 2C). Nitrogen incorporation into the carbon framework during the thermal condensation of urea and citric acid precursors was validated by the overall elemental composition (C 53%, N 18%, O 28%) of the C-dots. High-resolution deconvolution of the C 1s region revealed three major components at 285, 286, and 288 eV, corresponding to C–C/C═C (23 at%), C–O/C–N (9.4 at%), and C═O/COOH (20.85 at%) bonds, respectively (Fig. S2A, SI). The N 1s spectrum contained two peaks centered at 399 and 401 eV, corresponding to N–H or pyrrolic (15. 8 at%) and graphitic or protonated nitrogen species (N–C_3 or N^+–H, 2.1 at%), respectively (Fig. S2B, SI). Oxygen-related peaks at 531and 533 eV were associated with carbonyl (C═O, 24 at%) and hydroxyl (C–O, 4.3 at%) groups (Fig. S2C, SI). The coexistence of nitrogen and oxygen functional groups confirmed successful heteroatom doping and surface passivation, both of which enhance the PL properties of C-dots and their water dispersibility.[37,38]

Next, the suitability of C-dots as fluorescent reporters was verified by introducing pAbs into the C-dot solution and measuring the PL intensity of C-dots. A rapid decrease in PL intensity was observed within 15 s, which subsequently remained invariant for at least 2 h (Fig. 2D). Notably, the PL emission wavelength of C-dots exhibited no significant change in the presence of pAbs (Fig. S1F, SI). Carbon dots are rich in surface functional groups (*e.g.*, –OH or –COOH groups) interacting with the amino acid residues in pAbs (*e.g.*, –NH_2, or –COOH groups).[33,39] Quenching of PL of C-dots arises from a combination of static and dynamic mechanisms.[40] Static PL quenching occurs due to binding events at the C-dot surface, resulting in the formation of a non-fluorescent ground-state complex between the fluorophore and the quencher and leading to a reduced emission intensity without altering fluorescence lifetime.[40,41] Dynamic quenching arises from collisional interactions in the excited state, often mediated by energy or charge transfer processes. Fig. 2E shows the reduction in the average normalized PL intensity of C-dots, I/I_0, as a function of the mass concentration ratio of pAbs-to-C-dots ($C_{pAbs}/C_{C\text{-dot}}$), where I is the PL intensity of the C-dot sample after the addition of pAbs and I_0 is the initial PL intensity of C-dots before the addition of pAbs. For 20 ≤ $C_{pAbs}/C_{C\text{-dot}}$ ≤ 180 mg mg^{-1}, the value of I/I_0 decreased linearly from ~0.84 to 0.69 (Fig. 2E), while at $C_{pAbs}/C_{C\text{-dot}}$ > 180 mg mg^{-1}, the change in I/I_0 was not linear, with a minimum I/I_0 ≈ 0.25 was achieved at $C_{pAbs}/C_{C\text{-dot}}$ = 1350 mg mg^{-1}. Importantly, at a 96% purity designated by the vendor, the pAbs were identified as the primary contributor to PL quenching, while approximately 4% bovine serum albumin (BSA) impurity accounted for <2% of the total PL quenching (Fig. S3A, SI), confirming that the measured PL quenching was driven by non-specific

interactions of C-dots with pAbs. In addition, incubation of C-dots with one of the surface-protecting surfactants used in the present work (Kolliphor® P 188 Bio) did not alter the PL properties of C-dots (Fig. S3B–D, SI).

The interaction of C-dots with pAbs was further supported by the results of isothermal titration calorimetry (ITC) experiments. An exothermic binding profile was acquired when C-dots were added to a solution of pAbs (Fig. 2F), revealing notable interactions of pAbs with C-dots that directly caused the quenching of their PL intensity. In contrast, no measurable binding was detected between C-dots and Kolliphor® P 188 Bio under the same experimental conditions (Fig. S3E, SI).

To achieve the surface immobilization of C-dots for the next stage of this work, the surface of PDMS was modified with 3-(aminopropyl)triethoxysilane (APTES) by using vapor-phase silanization (Fig. 3A).[42] The details of the surface modification procedure are provided in the Experimental section. Fig. S4A–C, SI displays the XPS survey, C 1s, and N 1s spectra of the APTES-modified wafer prior to C-dot attachment. More specifically, the C 1s region (Fig. S4B) displayed the peaks consistent with the alkylsilane backbone, and the N 1s high-resolution spectrum (Fig. S4C) exhibits a dominant peak at 399 eV (5.16 at%), assigned to the terminal amine ($-NH_2$) group, a smaller peak at 400 eV, attributed to protonated amines ($-NH_3^+$), and a weak component at 401 eV, consistent with hydrogen-bonded or partially oxidized nitrogen species.[43–45] The existence of these peaks confirms the formation of the amino-terminated silane layer. Following this step, the APTES-modified surface was exposed for 12 h to an aqueous suspension of C-dots in deionized water. At pH 6.3, interfacial condensation between the protonated surface primary amines of APTES and deprotonated carboxyl groups of the C-dots in solution can yield covalent amide-bond linkages.[46–48] Computational and experimental studies have shown that alkoxysilane derivatives lower the activation barrier for amide bond formation by stabilizing key intermediates in the condensation pathway.[47–49] In addition, carboxylic acid groups on the C-dot surface can be further activated *via* hydrogen bonding with APTES, enabling amidation to proceed in the aqueous, mildly acidic environment. Moreover, the surface confinement of the APTES monolayer inherently increases the local effective concentration of reactive amine groups and lowers the entropic barrier for covalent coupling relative to the bulk solution. The XPS analysis of the surface of APTES-modified silicon wafer exposed to the solution of C-dots and rinsed with water confirmed the covalent attachment of C-dots, that is, a reduced silicon signal (Fig. S4D, SI) and prominent peaks in the C 1s (288 eV, 11.3 at%) (Fig. S4E, SI) and N 1s (400 eV, 9.2 at%) (Fig. S4F, SI) spectra, which were characteristic of amide carbonyl and nitrogen species, respectively.[50,51] In contrast, the non-modified silicon wafer exposed to C-dot solution and rinsed with water exhibited a stronger silicon substrate signal (Fig. S4G, SI), a weak carbon signal (Fig. S4H, SI) and low nitrogen content (2.28 at%) (Fig.

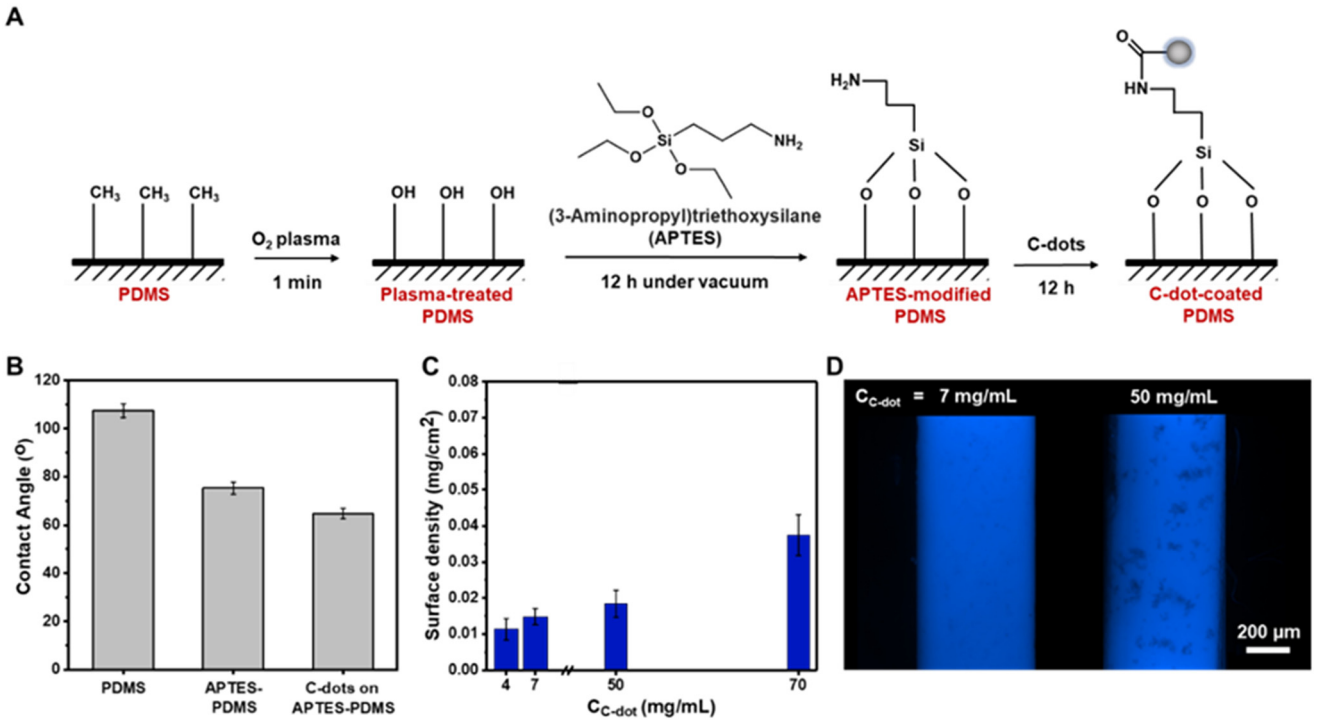

Fig. 3 Fabrication of C-dot-functionalized MF devices. (A) Workflow for the chemical modification of the surface of PDMS microchannels with C-dots. (B) Contact angle of water on the PDMS surfaces before and after surface modification. (C) Surface density of C-dots in the microchannel, plotted as a function of $C_{C\text{-}dot}$ in the solution. (D) Fluorescence microscopy images of the microchannel after modification at $C_{C\text{-}dot}$ of 7 and 50 mg mL^{-1}. Error bars represent mean ± standard deviation (n = 3 independent experiments). For the 70 mg mL^{-1} condition in (C), n = 2 was used.

S4I, SI), all of which were indicative of weak C-dot surface attachment. Collectively, these spectral features support the key role of APTES in facilitating the covalent surface immobilization of C-dots.

After modifying the PDMS surface with APTES and C-dots, it was rinsed to remove unattached or weakly attached C-dots (Fig. S5A, SI). The wetting contact angle of the PDMS surface decreased from 107 to 75° after being modified with APTES and further to 65° after functionalization with C-dots (Fig. 3B). Fluorescence microscopy imaging confirmed C-dot immobilization onto the APTES-modified PDMS surface, as indicated by the strong and uniform PL signal, with PL intensity increasing with the C-dot mass concentration ($C_{C\text{-}dot}$) (Fig. S5B, SI). Following the quantification of the C-dot surface density on the microchannel surface, as described in the Experimental section, the concentration $C_{C\text{-}dot}$ = 7 mg mL^{-1} was identified as optimal, leading to the surface density of C-dots of 0.015 ± 0.002 mg cm^2 (Fig. 3C). At $C_{C\text{-}dot}$ beyond this threshold (that is, 20–100 mg mL^{-1}), the nanoparticles formed surface aggregates, and their PL was self-quenched (Fig. 3D and S5B, SI). Overall, at $C_{C\text{-}dot}$ in the range of 4.0–100 mg mL^{-1} a significantly higher density of C-dots was found on the APTES-modified PDMS surface (Fig. S5B and S6A SI), in comparison with the non-modified surface to which the C-dots attached solely due to physical adsorption (Fig. S6B and S7, SI).

Adsorption of pAbs onto the microchannel surface functionalized with C-dots was monitored in real time during perfusion of the pAbs solution through the MF device shown in Fig. 4A. The MF device containing 12 parallel microchannels enabled the examination of pAbs adsorption from solutions with four pAbs concentrations, each in triplicate format. Each pAbs solution was perfused through the microchannel, with a time-dependent decrease in C-dot PL intensity monitored for 5 min. Fig. 4B shows representative variations in the I/I_0 value for the lowest and highest pAbs mass concentrations (C_{pAbs}), where I and I_0 are the PL intensities at a particular time point and 15 s after insertion of the pAbs solution in the MF device, respectively. Perfusion of the solution with C_{pAbs} = 300 mg mL^{-1} resulted in a rapid decline of I/I_0 to 0.43 within 1 min, corresponding to a 57% quenching of the initial PL signal, with the value of I/I_0 decreasing to 0.08 after 5 min. Following perfusion of the 10 mg mL^{-1} pAbs solution, the decrease in I/I_0 was more gradual, reaching 22% quenching after 5 min.

Fig. 4C shows a comparison of the reduction in the ratio of I/I_0 after 5 min perfusion of pAbs solutions with different concentrations through the MF device. Perfusion of the 10 mg mL^{-1} solution of pAbs resulted in a minimal reduction of I/I_0 to 0.78, only ~9% greater than the histidine baseline signal, thus indicating the sensitivity of the measurements in the present work. As the concentration of pAbs in the solution increased, a progressively greater PL quenching was observed, correlating with stronger pAbs adsorption.

Next, we focused on the evaluation of the surface-protecting performance of two antifouling compounds, Kolliphor® P 188 Bio and Kolliphor® PS 20. These experiments were performed using two protocols. In protocol 1, the microchannels were pre-treated with either Kolliphor® P 188 Bio or Kolliphor® PS 20. This step was followed by perfusion of the pAbs solution with a particular concentration (Fig. 5A and D). In protocol 2, a mixed solution of pAbs with Kolliphor® P 188 Bio or Kolliphor® PS 20 was perfused through a MF channel (Fig. 5B and E, respectively). The summaries of the results acquired using both protocols for pAbs solutions with different concentrations using Kolliphor® P 188 Bio and Kolliphor® PS 20 are shown in Fig. 5C and F, respectively.

In the experiment conducted using protocol 1, Kolliphor® P 188 Bio exhibited a weak anti-fouling effect, with the ratio I/I_0 decreasing to 0.83 and 0.20 after perfusion of 10 and 300 mg mL^{-1} pAbs for 300 s, respectively, compared to 0.78 and 0.08 measured in the microchannels not protected with this surfactant (Fig. 5A). A small difference in I/I_0 values between protected and non-protected microchannels indicated that surface pre-treatment with Kolliphor® P 188 Bio resulted in a

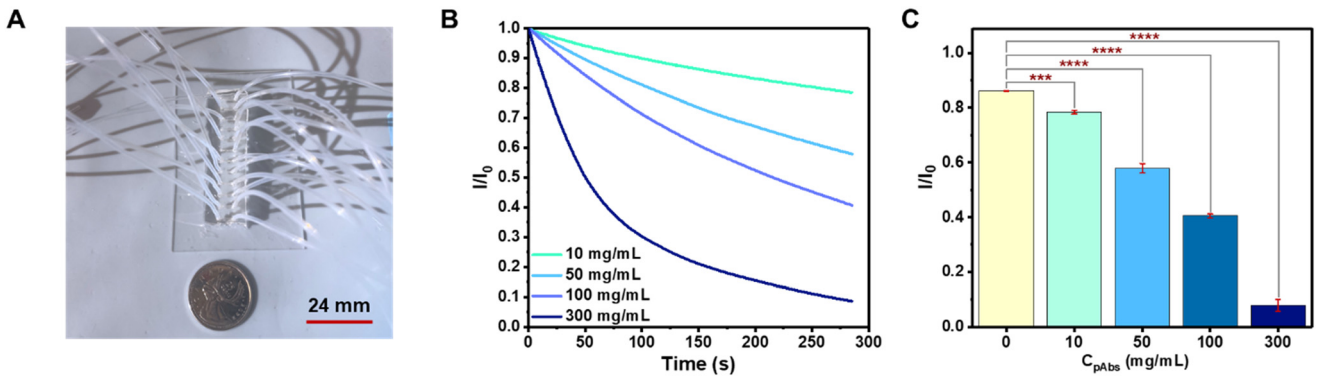

Fig. 4 Real-time fluorescence assay-based measurements of the adsorption of pAbs on PDMS within the MF platform. (A) Photograph of the fabricated MF device comprising 12 parallel channels, each with one inlet and one outlet connected to tubing for high-throughput analysis. (B) Time-dependent decay in I/I_0 during perfusion of pAbs in histidine buffer (pH = 6), showing increased quenching with higher concentrations of pAbs. (C) One-way ANOVA statistical analysis followed by Dunnett's test of the ratio I/I_0 at the end of 300 s perfusion showing statistically significant differences among groups ($p < 0.05$). Error bars represent mean ± standard deviation (n = 3 independent experiments).

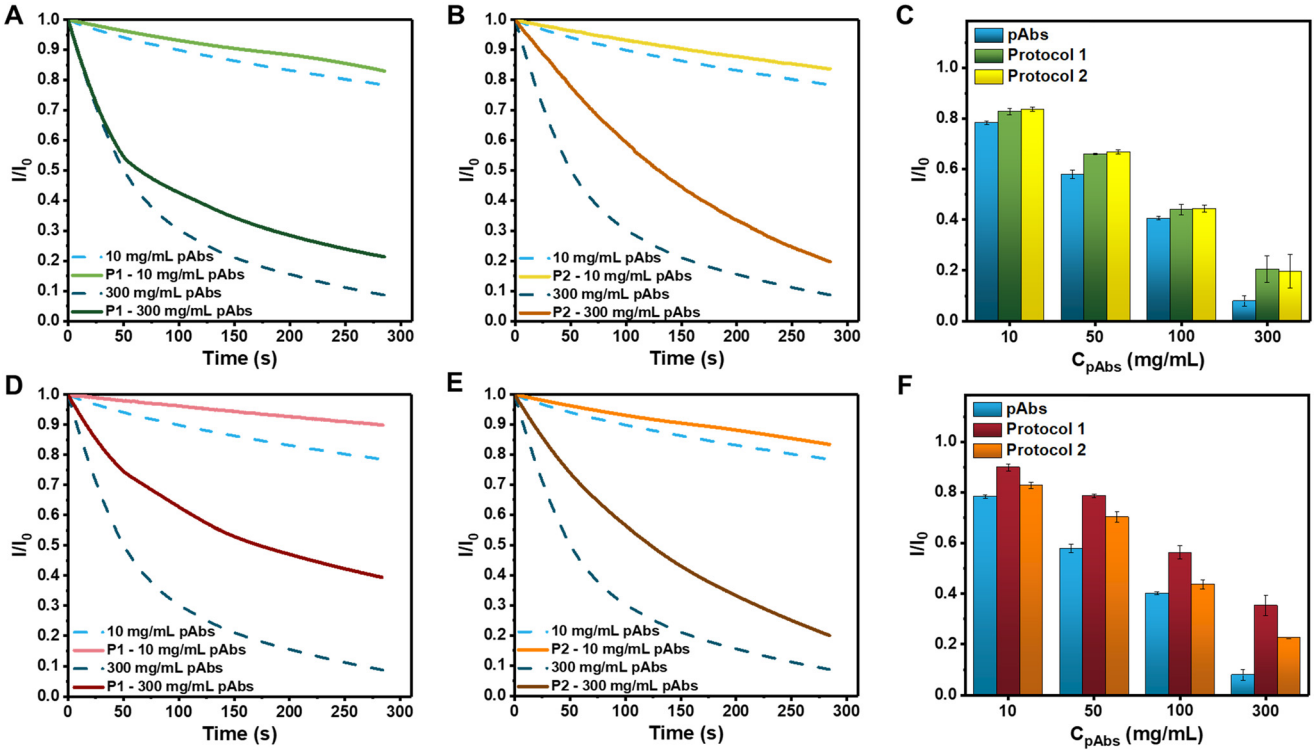

Fig. 5 Fluorescence assay-based evaluation of the surface-protecting performance of anti-fouling surfactants. Real-time monitoring of I/I_0 of surface-attached C-dots following perfusion of pAbs solution through microchannels protected with (A–C) Kolliphor® P188 Bio or (D–F) Kolliphor® PS 20. Panels A and D correspond to experiments performed using protocol 1; panels B and E correspond to experiments performed using protocol 2. Panels C and F present the steady-state I/I_0 value after 5 min perfusion of pAbs solution with different concentrations. Error bars represent mean ± standard deviation (n = 3 independent experiments).

minor surface protection from pAbs adsorption. In contrast, the results obtained for the microchannels protected with Kolliphor® PS 20 using the same protocol showed superior surface-protection, maintaining I/I_0 at 0.9 and 0.35 after perfusion of 10 and 300 mg mL^{-1} pAbs for 300 s, respectively (Fig. 5D). In experiments carried out using protocol 2, Kolliphor® P 188 Bio yielded I/I_0 values similar to those observed under protocol 1 (Fig. 5A and B), while the anti-fouling performance of Kolliphor® PS 20 was diminished, with I/I_0 decreasing to 0.83 and 0.23 following perfusion of 10 and 300 mg mL^{-1} pAbs for 300 s, respectively (Fig. 5E). These trends were consistent for pAbs solutions with all examined concentrations (Fig. 5C and F).

To complement and validate PL-based results obtained in the MF device, we performed pAbs adsorption studies using QCM-D experiments and Bradford assay. In the QCM-D experiments, we used PDMS-coated sensors functionalized with C-dots following the surface modification protocol applied to the PDMS surface in the MF channels. Prior to each measurement, baseline stabilization was performed by perfusing the histidine buffer through the QCM-D chamber for 1 h (Fig. S8A–D, SI), which was followed by the supply of a 1.7 mg mL^{-1} pAbs solution and a subsequent perfusion of the histidine buffer for 90 min to remove weakly adsorbed molecules. A decrease in the resonance frequency (Δf_7) was observed due to pAbs adsorption on both non-modified and APTES-modified PDMS surfaces, with or without C-dot functionalization (Fig. 6A). The adsorbed mass (Δm) of pAbs was calculated using the Sauerbrey model in eqn (1):[52]

$$\Delta m = \frac{-C \cdot \Delta f_n}{n}, \quad (1)$$

where C is the mass sensitivity constant (17.7 ng cm^{-2} Hz^{-1}) and n is the overtone number (7). The tested surfaces of PDMS and APTES-modified PDMS exhibited a similar large decrease in resonance frequency (Δf_7) (Fig. 6A), corresponding to a high degree of surface fouling by pAbs of 1548 ± 75 and 1622 ± 96 ng cm^{-2}, respectively (Fig. 6D). Surface modification with C-dots did not significantly change pAbs adsorption, resulting in a comparable surface coverage of 1624 ± 91 ng cm^{-2}. These results indicate that although introducing APTES functionalities onto PDMS decreased the hydrophobicity of the PDMS surface by approximately 39%, the surface adsorption behavior of pAbs was not affected. In addition, C-dots did not interfere with pAbs attachment to the PDMS surface and their function was to act solely as a fluorescent reporter. Moreover, this method accurately quantified the mass of adsorbed pAbs over a concentration range of 0.0003–1.7 mg mL^{-1} (Fig. S8E and F).

The QCM-D method was utilized to evaluate the surface-protecting performance of Kolliphor® P 188 Bio and Kolliphor® PS 20 using two experimental protocols described

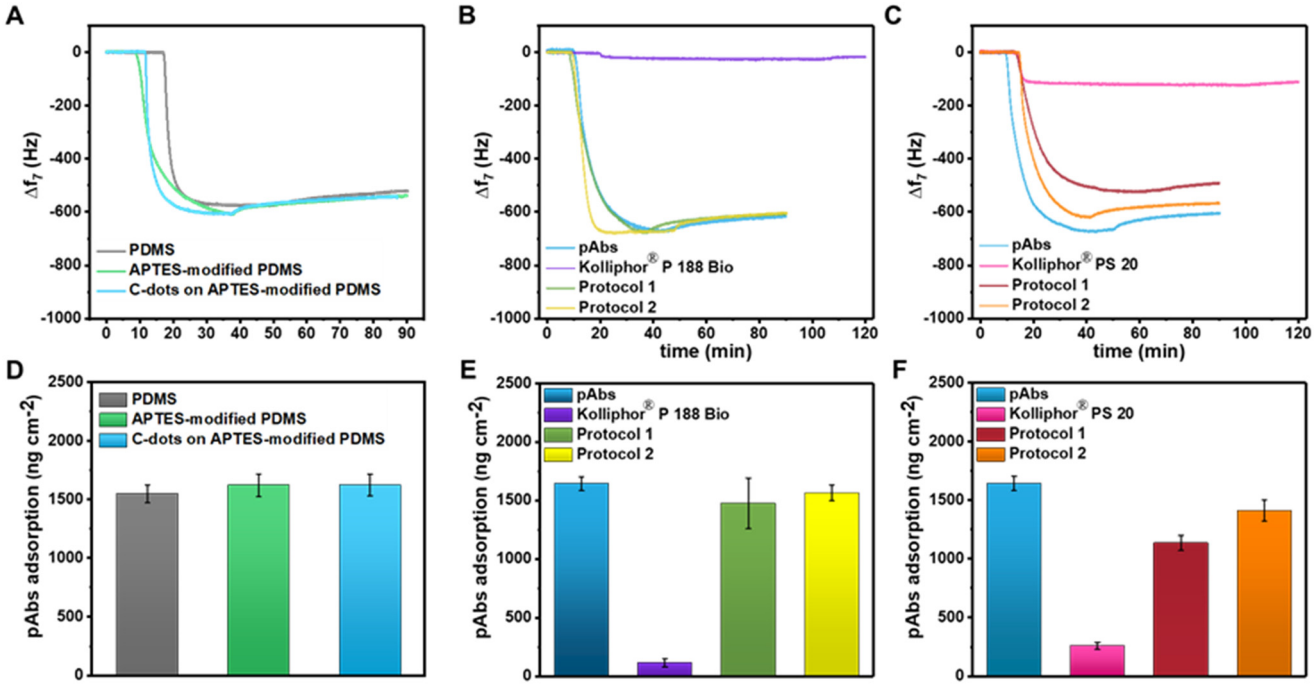

Fig. 6 QCM-D-based pAbs adsorption on PDMS-based sensor surfaces. Shifts in the resonance frequency (Δf_7) recorded during perfusion of pAbs over (A) unprotected PDMS-based surfaces, and (B and C) C-dot functionalized APTES–PDMS treated with Kolliphor® P 188 Bio and Kolliphor® PS 20, respectively. (D) Adsorption of pAbs to the non-modified and APTES-modified PDMS surface with or without functionalization with C-dots. (E and F) Adsorption of pAbs to the APTES-modified PDMS surface functionalized with C-dots and treated with Kolliphor® P 188 Bio (E) and Kolliphor® PS 20 (F), respectively. Error bars represent mean ± standard deviation (n = 3 independent experiments).

in the Methods section, involving surface pre-treatment with the anti-fouling surfactant in protocol 1 and co-perfusion of the mixture of pAbs with the surfactant in protocol 2. Fig. 6B shows that Kolliphor® P 188 Bio exhibited weak antifouling performance under both experimental conditions, signified by a strong shift in resonance frequency after perfusion of pAbs solution. In these experiments, the mass of adsorbed pAbs was comparable to those attached to the unprotected PDMS surface (Fig. 6E). In contrast, Kolliphor® PS 20 effectively suppressed fouling. The effect was stronger when the surface was pre-treated with the surfactant (protocol 1), as shown in Fig. 6C. Adsorption mass change was 1135 ± 63 ng cm^{-2}, that is, a ~31% reduction in pAbs adsorption occurred in comparison with the unprotected surface (Fig. 6F). Notably, the adsorbed mass of Kolliphor® PS 20 of 259 ± 29 ng cm^{-2} was two-fold greater than 114 ± 33 ng cm^{-2} determined for Kolliphor® P 188 Bio, indicating a stronger affinity of PS 20 toward the surface.

Secondly, the Bradford assay was done for experiments performed using protocol 1 and protocol 2. As summarized in Table 1, the strongest adsorption of pAbs occurred when the pAbs solution in histidine buffer was perfused through the non-protected microchannel, confirming the critical role of anti-fouling surfactants in suppressing nonspecific antibody binding. Surface treatment with Kolliphor® PS 20 (protocol 1) provided the most effective protection against pAbs adsorption. In contrast, premixing Kolliphor® PS 20 with the pAbs solution (protocol 2) resulted in an inferior surface protection compared to the pre-coating method in protocol 1, similar to that of Kolliphor® P 188 Bio. Nevertheless, in protocol 1, Kolliphor® PS 20 outperformed Kolliphor® P 188 Bio, for which a substantially higher adsorption of pAbs was observed.

We note that the concentrations of pAbs used in the QCM-D and Bradford methodologies were significantly lower than those applied in the MF fluorescence assay due to the intrinsic limitations of these approaches. Nevertheless, these

Table 1 Bradford assay results for pAbs adsorption to the microchannel surfaces

Experimental condition	C_{pAbs} recovered (mg mL^{-1})	C_{pAbs} adsorbed (mg mL^{-1})
Control	437 ± 44	1063 ± 44
Protocol 1 – Kolliphor® P 188 Bio	683 ± 46	817 ± 46
Protocol 2 – Kolliphor® P 188 Bio	547 ± 82	953 ± 82
Protocol 1 – Kolliphor® PS 20	986 ± 40	514 ± 40
Protocol 2 – Kolliphor® PS 20	620 ± 22	880 ± 22

two methods and the PL assay conducted in the MF experiments showed similar trends in the adsorption of pAbs onto the surface of PDMS and the examination of the anti-fouling performance of Kolliphor® P 188 Bio and Kolliphor® PS 20. This similarity validates the results obtained in the MF platform and leads to the following conclusions. First, increasing pAbs concentration consistently led to a stronger PL quenching, which correlated with higher adsorption detected by the QCM-D method, confirming that pAbs binding occurs on both the C-dot coating and the underlying PDMS surface. We hypothesize that pAbs bind to the PDMS surface in a flat-on orientation, driven by favorable hydrophobic interactions,[15,16] while the exposed fragment antigen-binding (Fab) regions can engage with the surface functional groups of C-dots by hydrogen bonding.[33] These intermolecular interactions likely perturb the emissive surface states of C-dots, resulting in an observable quenching of PL intensity.[33,34] Secondly, Kolliphor® P 188 Bio demonstrated an inferior surface-protecting effect, compared to Kolliphor® PS 20, in experiments performed using protocol 1. In experiments conducted under protocol 2, no significant differences were observed between the two surfactants across all tested antibody concentrations. These results indicate that for industrial applications, the efficiencies of Kolliphor® P 188 Bio and Kolliphor® PS 20 in preventing antibody adsorption to hydrophobic PDMS surfaces are comparable. The diminished performance of Kolliphor® PS 20 is likely due to the competitive adsorption between pAbs and Kolliphor® PS 20 to the PDMS surface, which hindered the formation of a densely packed, protective monolayer. In contrast, no statistically significant difference in surface protection was observed for Kolliphor® P 188 Bio in experiments performed with either protocol 1 or 2. Collectively, these results can be understood in terms of surfactant structure: a relatively low molecular weight Kolliphor® PS 20 packed densely, yielding a high surface coverage when used as a pre-treatment, but competed with pAbs adsorption from mixed solutions.[18,53,54] In contrast, Kolliphor® P 188 Bio, a significantly larger surfactant, anchored to the PDMS surface with a short polypropylene oxide block, which resulted in its low packing density and increased antibody access.[20,22] The large polyethylene oxide blocks further restricted the surface attachment of neighboring molecules due to steric repulsion, thus preventing the formation of the dense surfactant layer. Consequently, pre-treatment resulted in relatively low surface coverage for P 188 and hence, weaker anti-fouling performance, while co-perfusion conditions resulted in similar results compared to PS 20, showcasing the suitability of P 188 as an alternative surfactant to PS 20 in real-world formulations.

Importantly, the developed MF approach is designed to provide a high-throughput, concentration-dependent readout of pAbs adsorption at moderate-to-high concentrations, rather than precise kinetic parameter extraction at low pAbs concentrations, where techniques such as SPR or QCM-D are more appropriate. Table 2 shows that in comparison with QCM-D and SPR techniques, the MF platform offers advantages in multiplexing, speed, and sample size, requiring only 5 μL per experiment and ~5 min per experiment. In contrast, QCM-D and SPR, while highly sensitive at low concentrations, require longer acquisition times (~90 and ~35 min, respectively) and operate at lower throughput.[55,56]

Experimental

Materials

Bovine polyclonal IgG antibodies (96%, SDS-PAGE (IgG w/w Total Protein)) were supplied by MP Biomedicals, LLC, United States. Kolliphor® P 188 Bio with a molecular weight of 8500 g mol^{-1} and Kolliphor® PS 20 with a molecular weight of 1200 g mol^{-1} were supplied by BASF SE, Germany. Later in the text, these compounds are termed as "surfactants". Citric acid (ACS reagent grade, ≥99.5%, crystals), urea (ACS reagent grade, ≤0.001% heavy metals by ICP-OES, metal basis, 99.0–100.5%, solid), *N*,*N*-dimethylformamide (ACS reagent, ≥99.8%), petroleum ether (puriss. p.a., reag. Ph. Eur., high boiling, bp 50–70 °C), ethyl acetate (ACS reagent, ≥99.5%), (3-aminopropyl) triethoxysilane (99%), L-histidine (≥99% (TLC), ReagentPlus®), bovine serum albumin (heat shock fraction, protease free, fatty acid free, essentially globulin free, pH 7, ≥98%), 2-propanol (ACS reagent, ≥99.5%), hydrochloric acid (37%, ACS reagent), and ethanol (95%, ACS reagent) were purchased from Sigma-Aldrich, Canada. A Pierce™ Bradford Plus Protein Assay Reagent was purchased from Thermo Scientific, Canada. Sylgard 184 silicone elastomer base and PDMS were purchased from Dow Corning Corporation, United States. Deionized water (resistivity of 18.2 MΩ cm at

Table 2 Operational parameters of the MF method and QCM-D and SPR techniques

Parameter	MF method[a]	QCM-D[a]	SPR[55,56]
Total volume required (μL)	5	500	~500–1500
Working concentration range (mg mL^{-1})	10–300	3.4×10^{-4} – 0.17	1.68×10^{-5} – 1.0
Sample consumption (mg)	0.05–1.5	1.7×10^{-4} – 0.085	8.4×10^{-6} – 1.5
Real-time measurement	Yes	Yes	Yes
Throughput	High	Low	Medium–low
Time per run (min)	~5	~90	~15–25

[a] Based on the present work.

25 °C) was obtained from a Milli-Q Water Purification system.

Synthesis of C-dots

Blue-emissive C-dots were synthesized following a modified procedure reported elsewhere.[29] Briefly, 3 mmol citric acid and 10 mmol urea were dissolved in 10 mL of *N*,*N*-dimethylformamide under stirring for 30 min. The mixed solution was transferred into a stainless-steel autoclave reactor with a polytetrafluoroethylene (PTFE)-liner and was maintained at 140 °C for 4 h. Subsequently, the reaction mixture cooled down to room temperature and was centrifuged at 11 644*g* for 10 min to remove the solid residues. To separate the C-dots, the supernatant was decanted into a mixture of petroleum ether and ethyl acetate (1 : 1 v/v). Upon collection, the final product was placed overnight in a vacuum oven to evaporate the residual solvent and subsequently stored at −20 °C until further use.

Optical and structural characterization of C-dots

Aqueous dispersions of C-dots were prepared by transferring the nanoparticles into deionized water or 20 mM histidine buffer (pH = 6.0), followed by vortex-mixing for 30 s. PL spectra of C-dot solutions (Fig. S1B and C, SI) were collected using a Varian Cary Eclipse fluorescence spectrophotometer (Agilent Technologies, Santa Clara, CA, USA). The stability of C-dots was evaluated by comparing their initial PL spectra to those acquired after one week storage in 20 mM histidine buffer (pH = 6) (Fig. S1D and E SI).

TEM images were acquired with a Hitachi HT7700 microscope. Aqueous dispersions of C-dots were prepared at a concentration of 1 mg mL^{-1} and drop-casted onto carbon-coated copper grids for imaging. The average diameter of C-dots (Fig. S1A, SI) was determined by analyzing their TEM images using the ImageJ software (ImageJ, US National Institutes of Health, Bethesda, MA, USA).

X-Ray photoelectron spectroscopy

All samples for XPS analysis were prepared on 1 cm × 1 cm silicon wafer substrates. To characterize the surface chemistry of C-dots (Fig. S2, SI), two layers of a 50 mg mL^{-1} aqueous C-dot dispersion (40 μL per layer) were applied on the wafer, with each layer dried under nitrogen. The resulting C-dot-covered wafer was left overnight in a vacuum oven at room temperature. To prepare APTES-modified substrates, the silicon surface was first subjected to the vapor-phase silanization with APTES for 12 h, which was followed by thorough rinsing with isopropanol and deionized water (Fig. S4A–C, SI). A 7 mg mL^{-1} aqueous dispersion of C-dots was then drop-cast onto the APTES-modified substrate and left undisturbed overnight in the dark (Fig. S4D–F, SI). A control sample was prepared with C-dots deposited from 7 mg mL^{-1} solution on the non-modified silicon substrate (Fig. S4G–I, SI). Each sample was subsequently rinsed four times with 5 μL aliquots of deionized water.

Characterization of interactions of C-dots with pAbs

The interaction of C-dots and pAbs was studied using ITC. A 0.3 mg mL^{-1} dispersion of C-dots in 20 mM histidine buffer (pH = 6.0) was titrated into a 1 mg mL^{-1} pAbs solution in the same buffer. Each titration consisted of 19 sequential injections of 2 μL each, performed at 25 °C using a MicroCal PEAQ-ITC instrument (Malvern Instruments, UK). The resulting data were analyzed using the one-site binding model in the MicroCal PEAQ-ITC analysis software to evaluate the occurrence of binding interactions between C-dots and pAbs. As a control, the same methodology was used to study interactions of C-dots with Kolliphor® P188 Bio at the ratio of mass concentrations ($C_{\text{Kolliphor® P188 Bio}}/C_{\text{C-dot}}$) of 35 mg mg^{-1} (Fig. S3E, SI) and 160 mg mg^{-1} (Fig. S3F, SI).

To assess the change in the PL properties of C-dots upon their interactions with pAbs, the C-dots were added to a solution of pAbs prepared in 20 mM histidine buffer (pH = 6.0) and incubated at room temperature for 2 h. Starting from 15 s after C-dot addition, the variations in PL emission wavelength, λ_{em} (Fig. S1F, SI) and PL intensity of the C-dots were monitored for 2 h. The effect of the concentration of pAbs on PL quenching was examined by varying the $C_{\text{pAbs}}/C_{\text{C-dot}}$ ratio from 5.0 to 1350. To account for the contribution of approximately 4% BSA impurity which could be present in the 96% pAbs provided by the vendor, the same experiments were performed using BSA alone (Fig. S3A, SI). In addition, to confirm that surfactants do not alter the PL properties of C-dots, the experiments were repeated with Kolliphor® P 188 Bio (Fig. S3B–D, SI).

Fabrication of MF devices functionalized with C-dots

MF devices with 12 parallel microchannels with dimensions of 5 mm × 0.5 mm × 1 mm were fabricated in PDMS using a standard soft-lithography method.[57] The PDMS layers were plasma treated under O_2 for 1 min and functionalized with APTES by 12 h vapor deposition, followed by ethanol rinsing to remove unreacted silane. Two APTES-modified PDMS layers were plasma-treated for 1 min and brought into contact to seal the device. The MF channels were filled with 5 μL of an aqueous C-dot dispersion and incubated for 12 h, after which 20 μL of histidine buffer was perfused through the channels to remove non-attached C-dots. To determine the number of rinsing steps required for the complete removal of unattached or weakly attached C-dots, the waste solution collected from each 5 μL rinsing step was diluted with 45 μL of histidine buffer, transferred to a 96-well plate, and analyzed using a CLARIOstar Plus plate reader (BMG Labtech, Germany). The PL intensity of each rinse solution was compared to that of the histidine buffer control (Fig. S5A, SI). Rinsed microchannels were examined using a Nikon Ti2 fluorescence microscope (Nikon, Japan) (Fig. S5B, SI). To optimize the $C_{\text{C-dot}}$ for device functionalization, the microchannels were filled with C-dot dispersions at 4.0, 7.0, 10, 20, 30, 50, 70, or 100 mg mL^{-1}, incubated for 12 h, and rinsed with four 5 μL perfusions of histidine buffer. The

optimal $C_{\text{C-dot}}$ value was identified as the lowest concentration producing a strong and stable PL signal without visible C-dot aggregation leading to PL self-quenching.

Quantifying surface density of C-dots on the MF channels

The coverage of the PDMS surface with C-dots was determined for the microchannels exposed to solutions of varying $C_{\text{C-dot}}$. After 12 h incubation, the supernatant, together with four sequential 5 μL rinsing aliquots were collected, diluted to 1 mL, and analyzed using a Varian Cary Eclipse fluorescence spectrophotometer. To quantify the surface coverage, the PL intensity of this solution was measured and converted to mass concentration using a calibration curve of PL intensity *vs.* C-dot concentrations in the solution (Fig. S6C, SI). The mass of surface-attached C-dots per unit surface area of the microchannel was subsequently determined as yielding the surface density of immobilized C-dots ($SD_{\text{C-dot}}$) in the microchannel corresponding to each $C_{\text{C-dot}}$, where $m_{\text{C-dot\_total}}$ is the initial mass of C-dots in the solution introduced into the channel, $m_{\text{C-dot\_unattached}}$ is the mass of non-attached or weakly adsorbed C-dots in the eluted solution, and SA is the surface area of the microchannel (Fig. S6A and B, SI). Fig. S7, SI shows the images of the microchannel surfaces without the modification with APTES, which were exposed to the solutions of different $C_{\text{C-dot}}$ and subsequently rinsed with deionized water as before.

$$SD_{\text{C-dot}} = \frac{m_{\text{C-dot\_total}} - m_{\text{C-dot\_unattached}}}{SA}, \quad (2)$$

Contact angle measurements

The contact angle of water on the PDMS, APTES-modified PDMS, and APTES-modified PDMS surface functionalized with C-dots was measured using the sessile droplet method, where 3 different areas of the PDMS sheet were assessed with a drop shape analyzer DSA100E (Kruss Scientific, Germany). The average values of the three contact angle measurements were obtained for each surface.

MF fluorescence assay

To evaluate the degree of PL quenching of surface-attached C-dots due to their interactions with pAbs, a solution of histidine buffer containing varying C_{pAbs} was perfused through the microchannel at a flow rate of 2 μL min^{-1}. During perfusion, a video of the region of interest (ROI) measuring 100 × 100 pixels (0.073 mm × 0.073 mm) and located at the center of the microchannel was recorded for 5 min using the Nikon Ti2 fluorescence microscope. A small but measurable contribution of pAbs autofluorescence (Fig. S9, SI) was accounted by using this PL signal as a background.

Modifying the PDMS microchannels by vapor-phase APTES silanization ensured surface functionalization across the enclosed geometry of the microchannels, including their sidewalls, *via* gas-phase diffusion of the silane. Subsequent C-dot immobilization produced a continuous interface, evidenced by spatially uniform PL intensity along the microchannel surface confirmed by examining 3 ROIs, as shown in Fig. S10, SI. Image acquisition was performed by extracting individual frames from the recorded videos and analyzing the change in PL intensity over time using the NIS-Elements AR software (Nikon, Japan) (Fig. S10, SI).

Evaluation of surface-protecting performance of surfactants

To assess the antifouling performance of Kolliphor® P 188 Bio and Kolliphor® PS 20, their 0.05% w/v solutions were prepared in histidine buffer. In experiments carried out by protocol 1, a surfactant solution was introduced into a C-dot-functionalized microchannel and incubated for 1 h, which was followed by perfusion of histidine buffer through the channel. Next, a solution of pAbs in histidine buffer was perfused through the protected microchannel, and the change in PL intensity of C-dots was monitored by fluorescence microscopy. In experiments conducted using protocol 2, a mixture of the surfactant in solution with pAbs at a surfactant concentration of 0.05% w/v was perfused through a microchannel and the decay in PL intensity of surface-attached C-dots was monitored by fluorescence microscopy.

QCM-D experiments

Adsorption of pAbs on C-dot-modified PDMS quartz crystal sensor discs (BL-QSX 348, 5 MHz) was characterized using QCM-D following a modified procedure reported elsewhere.[20] The PDMS-coated sensors were functionalized with C-dots using the immobilization protocol employed for the functionalization of the MF channels. The PDMS-coated quartz sensors were cleaned by repeated rinsing with isopropanol and deionized water, followed by drying under nitrogen. The cleaned sensors were plasma treated in O_2 for 60 s and subsequently subjected to vapor-phase silanization with APTES for 12 h under vacuum. Excess APTES was removed by thorough rinsing of the surface with isopropanol and deionized water, and the sensors were dried under nitrogen. An aqueous dispersion of C-dots (7 mg mL^{-1}) was applied to the APTES-modified sensor surface and dried overnight in the dark. Non-bound C-dots were removed by rinsing with deionized water. The sensors were dried and assembled into the QCM-D module (Q-Sense E1, Biolin Scientific, Sweden). All experiments were performed at 22 °C. Baseline stabilization was achieved by the initial perfusion of 20 mM histidine (pH = 6.0) at 10 μL min^{-1} for 1 h using a peristaltic pump (Ismatec IPC-N4) connected to the sensor chamber (Fig. S8A–D, SI). After stabilization, 0.5 mL of pAbs solution in histidine buffer was perfused past the sensor, and the change in resonance frequency at the 7th overtone (Δf_7) was monitored over time (Fig. S8E, SI). Weakly bound pAbs were removed by 90 min perfusion of histidine buffer through the sensor chamber. The same protocol was used for

adsorption studies on the non-modified and C-dot-modified PDMS surfaces, as well as the generation of a calibration graph of the mass of adsorbed pAbs over a concentration range of 0.0003–1.7 mg mL^{-1} (Fig. S8F, SI). Surface protection studies using Kolliphor® P 188 Bio and Kolliphor® PS 20 were performed using two protocols. In protocol 1 experiments, 1 mL of the 0.05% (w/v) solution of the anti-fouling surfactant in histidine buffer was perfused immediately after baseline stabilization, followed by perfusion of the histidine buffer for 120 min. Subsequently, 0.5 mL of 0.17 mg mL^{-1} pAbs solution was perfused, followed by perfusion of the histidine buffer for 90 min. In protocol 2 experiments, a mixture of pAbs (0.17 mg mL^{-1}) and the anti-fouling surfactant (0.05% w/v) was perfused following initial baseline stabilization and terminated with perfusion of the final histidine rinsing step at 90 min.

Bradford assay

The concentration of pAbs in the solution eluted from the microchannels pre-treated with surface-protecting surfactants was quantified using the Bradford assay. A 5 μL aliquot of the recovered pAbs solution in histidine buffer was transferred into a 48-well plate filled with 300 μL of Bradford reagent. Histidine buffer alone and a 1.5 mg mL^{-1} pAbs solution perfused through unprotected MF channels served as negative and positive controls, respectively. Following a 10 min incubation to allow completion of the brown-to-blue colorimetric transition, the absorbance of the solution at 595 nm was recorded using the CLARIOstar Plus plate reader (BMG Labtech, Germany). The concentration of pAbs in the eluted solution was determined using the calibration graph constructed by plotting the absorbance of solutions with different C_{pAbs} in the histidine buffer, which contained the Bradford reagent (Fig. S11A, SI). Importantly, Kolliphor® P 188 Bio alone at the concentration of 0.05% w/v did not cause any change in the Bradford reagent (Coomassie Brilliant Blue) signal, confirming that the observed color shift originated solely from pAbs binding (Fig. S11B, SI). In contrast, Kolliphor® PS 20 (0.05% w/v) caused an increase in absorbance of the Bradford reagent. Therefore, its contribution was subtracted to ensure that the final absorbance values reflected only pAbs concentration.

Conclusions

In summary, a fluorescence assay based on C-dot photoluminescent reporters operating within an MF platform was developed for the real time studies of antibody adsorption from solutions onto the PDMS surface. Covalent immobilization of C-dots on the surface of APTES-functionalized PDMS microchannels provided a stable PL signal with the intensity reducing with pAbs adsorption. The method demonstrated the sensitivity and reproducibility across a wide range of pAbs concentrations, with the results consistent with independent QCM-D and Bradford analyses. Collectively, the results of this work validate our MF fluorescence assay as a reliable and accurate platform for studying pAbs adsorption and evaluation of the performance of surface-protecting surfactants. Our findings show that Kolliphor® PS 20 is superior to Kolliphor® P 188 Bio as a surface-protecting surfactant if it is used as a pre-treatment to prevent antibody adsorption to hydrophobic surfaces; meanwhile, using it in a mixture with the antibody molecules, both surfactants exhibit similar performance in preventing the adsorption of antibody molecules. The developed platform offers a high-throughput strategy for evaluating surface fouling with proteins and screening surface-protecting compounds in real-time with a broad potential for the rational design of anti-biofouling interfaces. The advantage of the MF strategy over the QCM-D methodology originates from the small antibody amount needed for adsorption studies, shorter time scales for such studies, and evaluation of the effect of surface-protecting compounds at high antibody concentrations (>100 mg mL^{-1}), which is representative of real-world therapeutic formulations. While the present study focuses on pAbs and two practically relevant surfactants, additional experiments with other proteins, including monoclonal antibodies, would further validate platform generality. It can be expected that the MF platform will be extended to studies of adsorption of a broad range of proteins, excipients, and emerging anti-fouling materials, supporting accelerated development of next-generation therapeutic antibody sensing and engineering strategies.

Abbreviations

FDA	US Food and Drug Administration
EMA	European Medicines Agency
IgG	immunoglobulin G
PDMS	polydimethylsiloxane
SPR	surface plasmon resonance
QCM-D	quartz crystal microbalance with dissipation monitoring
MF	microfluidic
PL	photoluminescence
C-dots	carbon dots
pAbs	polyclonal bovine IgG antibodies
TEM	transmission electron microscopy
XPS	X-ray photoelectron spectroscopy
$C_{pAbs}/C_{C\text{-}dot}$	mass concentration ratio of pAbs-to-C-dots
BSA	bovine serum albumin
ITC	isothermal titration calorimetry
APTES	3-(aminopropyl)triethoxysilane
$C_{C\text{-}dot}$	C-dot mass concentration
C_{pAbs}	pAbs mass concentration
Fab	fragment antigen-binding
PTFE	polytetrafluoroethylene
$C_{Kolliphor®\ P\ 188\ Bio}/C_{C\text{-}dot}$	mass concentration ratio of Kolliphor® P 188 Bio-to-C-dots
ROI	region of interest

Author contributions

All authors have given approval to the final version of the manuscript. Y. T. and B. M. B.-P. contributed equally to the experimental work, and E. K. supervised the project. Y. T. and E. K. drafted and revised the manuscript with the help of N. L., O. Z., and D. A. R. All authors contributed to the scientific discussion.

Conflicts of interest

There are no conflicts of interest to declare.

Data availability

The data supporting this article have been included as part of the supplementary information (SI).

Supplementary information: the file includes C-dot size distribution, PL properties, concentration dependence and stability; XPS characterization of C-dot surface chemistry; fluorescence spectra and ITC analysis during interactions of C-dots with BSA and Kolliphor® P 188 Bio; XPS confirmation of covalent C-dot attachment to APTES-modified surfaces; fluorescence validation of C-dot immobilization in PDMS microchannels; quantification of C-dot surface density on modified and non-modified microchannels; fluorescence microscopy of non-modified PDMS channels; QCM-D validation of pAbs adsorption on C-dot functionalized PDMS; pAbs autofluorescence contribution; spatial uniformity of PL along microchannels; Bradford assay calibration curve and controls. See DOI: https://doi.org/10.1039/d6lc00197a.

Acknowledgements

The authors acknowledge the support for the research described in this study from the BASF Corporation and the Natural Sciences and Engineering Research Council of Canada (NSERC) Alliance Program. The authors thank the Centre for Research and Applications in Fluidic Technologies (CRAFT) at the University of Toronto for their assistance in confocal microscopy. The authors would also like to thank the Open Centre for Characterization of Advanced Materials (OCCAM) at the University of Toronto for their assistance in the characterization of the C-dot surface chemistry and of the surface immobilization of C-dots to substrates by X-ray photoelectron spectroscopy. The authors further thank the Structural and Biophysical Core Facility at SickKids Hospital for their assistance in the analysis of binding interactions using isothermal titration calorimetry.

References

1 A. Teniou, A. Rhouati and J.-L. Marty, Recent Advances in Biosensors for Diagnosis of Autoimmune Diseases, *Sensors*, 2024, **24**, 1510.
2 M. J. Kim, I. Haizan, M. J. Ahn, D. H. Park and J. H. Choi, Recent Advances in Lateral Flow Assays for Viral Protein Detection with Nanomaterial-Based Optical Sensors, *Biosensors*, 2024, **14**, 197.
3 S. Zinn, R. Vazquez-Lombardi, C. Zimmermann, P. Sapra, L. Jermutus and D. Christ, Advances in Antibody-Based Therapy in Oncology, *Nat. Cancer*, 2023, **4**, 165–180.
4 H. Ausserwöger, G. Krainer, T. J. Welsh, N. Thorsteinson, E. Csilléry, T. Sneideris, M. M. Schneider, T. Egebjerg, G. Invernizzi, T. W. Herling, N. Lorenzen and T. P. J. Knowles, Surface Patches Induce Nonspecific Binding and Phase Separation of Antibodies, *Proc. Natl. Acad. Sci. U. S. A.*, 2023, **120**, e2210332120.
5 R.-M. Lu, Y.-C. Hwang, I.-J. Liu, C.-C. Lee, H.-Z. Tsai, H.-J. Li and H.-C. Wu, Development of Therapeutic Antibodies for the Treatment of Diseases, *J. Biomed. Sci.*, 2020, **27**, 1.
6 X.-Z. Wang, V. W. Coljee and J. A. Maynard, Back to the Future: Recombinant Polyclonal Antibody Therapeutics, *Curr. Opin. Chem. Eng.*, 2013, **2**, 405–415.
7 P. J. Carter and A. Rajpal, Designing Antibodies as Therapeutics, *Cell*, 2022, **185**, 2789–2805.
8 G. Vidarsson, G. Dekkers and T. Rispens, IgG Subclasses and Allotypes: From Structure to Effector Functions, *Front. Immunol.*, 2014, **5**, 520.
9 E. Sahin and S. Deshmukh, Challenges and Considerations in Development and Manufacturing of High Concentration Biologics Drug Products, *J. Pharm. Innov.*, 2020, **15**, 255–267.
10 M. Desai, A. Kundu, M. Hageman, H. Lou and D. Boisvert, Monoclonal Antibody and Protein Therapeutic Formulations for Subcutaneous Delivery: High-Concentration, Low-Volume vs. Low-Concentration, High-Volume, *mAbs*, 2023, **15**, 2285277.
11 S. Saurabh, Q. Zhang, Z. Li, J. M. Seddon, C. Kalonia, J. R. Lu and F. Bresme, Mechanistic Insights into the Adsorption of Monoclonal Antibodies at the Water/Vapor Interface, *Mol. Pharmaceutics*, 2024, **21**, 704–717.
12 I. Ghosh, H. Gutka, M. E. Krause, R. Clemens and R. S. Kashi, A Systematic Review of Commercial High-Concentration Antibody Drug Products Approved in the US: Formulation Composition, Dosage Form Design, and Primary Packaging Considerations, *mAbs*, 2023, **15**, 2205540.
13 P. Hollowell, Z. Li, X. Hu, S. Ruane, C. Kalonia, C. F. Walle and J. R. Lu, Recent Advances in Studying Interfacial Adsorption of Bioengineered Monoclonal Antibodies, *Molecules*, 2020, **25**, 2047.
14 S. S. Wang, Y. S. Yan and K. Ho, US FDA-Approved Therapeutic Antibodies with High-Concentration Formulation: Summaries and Perspectives, *Antibiot. Ther.*, 2021, **4**, 262–272.
15 H. Ausserwöger, M. M. Schneider, T. W. Herling, P. Arosio, G. Invernizzi, T. P. J. Knowles and N. Lorenzen, Non-Specificity as the Sticky Problem in Therapeutic Antibody Development, *Nat. Rev. Chem.*, 2022, **6**, 844–861.
16 S. Ruane, Z. Li, P. Hollowell, A. Hughes, J. Warwicker, J. R. P. Webster, C. F. Walle, C. Kalonia and J. R. Lu, Investigating

the Orientation of an Interfacially Adsorbed Monoclonal Antibody and Its Fragments Using Neutron Reflection, *Mol. Pharmaceutics*, 2023, **20**, 1643–1656.
17 Y. Razvag, V. Gutkin and M. Reches, Probing the Interaction of Individual Amino Acids with Inorganic Surfaces Using Atomic Force Spectroscopy, *Langmuir*, 2013, **29**, 10102–10109.
18 K. Shen, X. Hu, Z. Li, M. Liao, Z. Zhuang, S. Ruane, Z. Wang, P. Li, S. Micciulla, N. Kasinathan, C. Kalonia and J. R. Lu, Competitive Adsorption of a Monoclonal Antibody and Nonionic Surfactant at the PDMS/Water Interface, *Mol. Pharmaceutics*, 2023, **20**, 2502–2512.
19 A. Saha, S. Nir and M. Reches, Amphiphilic Peptide with Dual Functionality Resists Biofouling, *Langmuir*, 2020, **36**, 4201–4206.
20 N. Löw, C. Schneider, M. M. Zegota, A. Grabarek, E. Corradini, G. Schuster, M. M. Roskamp, F. Guth, A. Hawe and M. Kellermeier, Physicochemical Comparison of Kolliphor HS 15, ELP, and Conventional Surfactants for Antibody Stabilization in Biopharmaceutical Formulations, *Mol. Pharmaceutics*, 2025, **22**, 4890–4908.
21 Z. Zhang, A. M. Woys, K. Hong, C. Grapentin, T. A. Khan, I. E. Zarraga, N. J. Wagner and Y. Liu, Adsorption of Non-Ionic Surfactant and Monoclonal Antibody on Siliconized Surface Studied by Neutron Reflectometry, *J. Colloid Interface Sci.*, 2021, **584**, 429–438.
22 K. Soeda, M. Fukuda, M. Takahashi, H. Imai, K. Arai, S. Saitoh, R. S. K. Kishore, N. S. Oltra, J. Duboeuf, D. Hashimoto and Y. Yamanaka, Impact of Poloxamer 188 Material Attributes on Proteinaceous Visible Particle Formation in Liquid Monoclonal Antibody Formulations, *J. Pharm. Sci.*, 2022, **111**, 2191–2200.
23 A. Sperry, D. Imhoff, J. Traunfeld, S. Gundagari, K. Smaga and G. Singh, A Case Study Demonstrating the Importance of Glass Vial Selection for Parenteral Pharmaceutical Products, *J. Pharm. Sci.*, 2024, **113**, 2974–2980.
24 A. R. Patel, K. K. Kanazawa and C. W. Frank, Antibody Binding to a Tethered Vesicle Assembly Using QCM-D, *Anal. Chem.*, 2009, **81**, 6021–6029.
25 M. C. Dixon, Quartz Crystal Microbalance with Dissipation Monitoring: Enabling Real-Time Characterization of Biological Materials and Their Interactions, *J. Biomol. Tech.*, 2008, **19**, 151–158.
26 Y. P. Zhang, E. Lobanova, A. Dworkin, M. Furlepa, W. S. Yang, M. Burke, J. X. Meng, N. Potter, R. L. Sala, L. Kahanawita, F. Layburn, O. A. Scherman, C. H. Williams-Gray and D. Klenerman, Improved Imaging Surface for Quantitative Single-Molecule Microscopy, *ACS Appl. Mater. Interfaces*, 2024, **16**, 37255–37264.
27 T. Becherer, C. Grunewald, V. Engelschalt, G. Multhaup, T. Risse and R. Haag, Polyglycerol-Based Coatings to Reduce Non-Specific Protein Adsorption in Sample Vials and on SPR Sensors, *Anal. Chim. Acta*, 2015, **867**, 47–55.
28 A. Kroning, A. Furchner, D. Aulich, E. Bittrich, S. Rauch, P. Uhlmann, K. J. Eichhorn, M. Seeber, I. Luzinov, S. M. Kilbey, B. S. Lokitz, S. Minko and K. Hinrichs, In Situ Infrared Ellipsometry for Protein Adsorption Studies on Ultrathin Smart Polymer Brushes in Aqueous Environment, *ACS Appl. Mater. Interfaces*, 2015, **7**, 12430–12439.
29 X. Miao, D. Qu, D. Yang, B. Nie, Y. Zhao, H. Fan and Z. Sun, Synthesis of Carbon Dots with Multiple Color Emission by Controlled Graphitization and Surface Functionalization, *Adv. Mater.*, 2018, **30**, 1704740.
30 F. Yan, Z. Sun, H. Zhang, X. Sun, Y. Jiang and Z. Bai, The Fluorescence Mechanism of Carbon Dots, and Methods for Tuning Their Emission Color: A Review, *Microchim. Acta*, 2019, **186**, 583.
31 J. Yang, X. He, L. Chen and Y. Zhang, The Selective Detection of Galactose Based on Boronic Acid Functionalized Fluorescent Carbon Dots, *Anal. Methods*, 2016, **8**, 8345–8351.
32 Y. Ma, S. Nouri, D. A. Pham, A. Ziyaeyan, Z. Chen, S. Morozova, M. Chekini, X. Banquy, V. Adibnia, S. Viswanathan and E. Kumacheva, Phytoglycogen Nanolubricants with Extended Retention Time in Joints, *Adv. Funct. Mater.*, 2025, **35**, 2413525.
33 Z. Chen, J. Wang, H. Miao, L. Wang, S. Wu and X. Yang, Fluorescent Carbon Dots Derived from Lactose for Assaying Folic Acid, *Sci. China: Chem.*, 2016, **59**, 487–492.
34 Q. Wang, M. Wang, L. Zheng, Y. She, J. Wang, M. Jia and A. M. A. El-Aty, BSA–Carbon Dots: A Promising "Off–On" Fluorescence Probe for Detecting Glyphosate Residues in Agricultural Products, *Carbon Lett.*, 2023, **33**, 1935–1945.
35 M. Righetto, A. Privitera, I. Fortunati, D. Mosconi, M. Zerbetto, M. L. Curri, M. Corricelli, A. Moretto, S. Agnoli, L. Franco, R. Bozio and C. Ferrante, Spectroscopic Insights into Carbon Dot Systems, *J. Phys. Chem. Lett.*, 2017, **8**, 2236–2242.
36 B. Yang, R. Jelinek and Z. Kang, Current Progress in Carbon Dots: Synthesis, Properties and Applications, *Mater. Chem. Front.*, 2020, **4**, 1287–1288.
37 J. D. Stachowska, A. Murphy, C. Mellor, D. Fernandes, E. N. Gibbons, M. J. Krysmann, A. Kelarakis, E. Burgaz, J. Moore and S. G. Yeates, A Rich Gallery of Carbon Dots Based Photoluminescent Suspensions and Powders Derived by Citric Acid/Urea, *Sci. Rep.*, 2021, **11**, 10554.
38 L. Li and T. Dong, Photoluminescence Tuning in Carbon Dots: Surface Passivation or/and Functionalization, Heteroatom Doping, *J. Mater. Chem. C*, 2018, **6**, 7944–7970.
39 J. S. A. Devi, S. M. Anju, G. M. Lekha, R. S. Aparna and S. George, Luminescent Carbon Dots versus Quantum Dots and Gold Nanoclusters as Sensors, *Nanoscale Horiz.*, 2024, **9**, 1683–1702.
40 F. Zu, F. Yan, Z. Bai, J. Xu, Y. Wang, Y. Huang and X. Zhou, The Quenching of the Fluorescence of Carbon Dots: A Review on Mechanisms and Applications, *Microchim. Acta*, 2017, **184**, 1899–1914.
41 K. F. Kayani, S. J. Mohammed, D. Ghafoor, M. K. Rahim and H. R. Ahmed, Carbon Dot as Fluorescence Sensor for Glutathione in Human Serum Samples: *A Review*, *Mater. Adv.*, 2024, **5**, 4618–4633.
42 E. Ayoub, F. Dawaymeh, M. Khaleel and N. Alamoodi, Enhancing Hydrophilicity of PDMS Surfaces through

Graphene Oxide Deposition, *J. Mater. Sci.*, 2024, **59**, 8205–8219.

43 M. Dong, X. Wu, Y. Cai, Y. Mei, X. Peng, S. Zhang, Y. Wu, D. Zhang, C. Yang, J. Zou and P. Si, Five-Coordinated Copper Multifunctional Hydrogel for Human-Machine Interface, *Chem. Eng. J.*, 2025, **526**, 171117.

44 Y. Wang, M. Lieberman, Q. Hang and G. Bernstein, Selective Binding, Self-Assembly and Nanopatterning of the Creutz–Taube Ion on Surfaces, *Int. J. Mol. Sci.*, 2009, **10**, 533–558.

45 R. G. Acres, A. V. Ellis, J. Alvino, C. E. Lenahan, D. A. Khodakov, G. F. Mehta and G. G. Andersson, Molecular Structure of 3-Aminopropyltriethoxysilane Layers Formed on Silanol-Terminated Silicon Surfaces, *J. Phys. Chem. C*, 2012, **116**, 6289–6297.

46 R. M. Figueiredo, J.-S. Suppo and J.-M. Campagne, Nonclassical Routes for Amide Bond Formation, *Chem. Rev.*, 2016, **116**, 12029–12122.

47 M. C. D'Amaral, N. Jamkhou and M. J. Adler, Efficient and Accessible Silane-Mediated Direct Amide Coupling of Carboxylic Acids and Amines, *Green Chem.*, 2021, **23**, 288–295.

48 J. J. Davies, D. C. Braddock and P. D. Lickiss, Silicon Compounds as Stoichiometric Coupling Reagents for Direct Amidation, *Org. Biomol. Chem.*, 2021, **19**, 6746–6760.

49 B. Hu, Y. Y. Jiang, R. X. Zhang, Q. Zhang, P. Liu, T. T. Liu and S. Bi, The Mechanism and Structure–Activity Relationship of Amide Bond Formation by Silane Derivatives: A Computational Study, *Org. Biomol. Chem.*, 2019, **17**, 9232–9242.

50 X. Shi, Q. Zhang, Z. Ma, S. Liu, D. Li and D. Jiang, Enhanced Charge Separation Endowed by Perylene Diimide Polymers Decorated N Vacancy on Carbon Nitride S-Scheme Heterojunction for Efficient Photocatalytic N_2 Fixation, *ChemSusChem*, 2025, **18**, e202501477.

51 Y. Xu, Y. Wang, L. Guan, P. Zhang, Z. Wu, S. Jehan, C. Peng, B. Yang, Y. Yao, P. Zhuang, W. Zhou, W. W. Zhang and H. Wang, Precision Drug Delivery for Multifunctional Treatment of Abdominal Aortic Aneurysm Using Bioactive Tea Polyphenol Nanoparticles, *ACS Appl. Mater. Interfaces*, 2025, **17**, 35080–35098.

52 A. D. Easley, T. Ma, C. I. Eneh, J. Yun, R. M. Thakur and J. L. Lutkenhaus, A Practical Guide to Quartz Crystal Microbalance with Dissipation Monitoring of Thin Polymer Films, *J. Polym. Sci.*, 2022, **60**, 1090–1104.

53 J. Whiteley, L. J. Waters, J. Humphrey and S. A. Mellor, Thermodynamic Investigation into Protein–Excipient Interactions Involving Different Grades of Polysorbate 20 and 80, *J. Therm. Anal. Calorim.*, 2024, **135**, 1–11.

54 A. D. Grabarek, U. Bozic, J. Rousel, T. Menzen, W. Kranz, K. Wuchner, W. Jiskoot and A. Hawe, What Makes Polysorbate Functional? Impact of Polysorbate 80 Grade and Quality on IgG Stability during Mechanical Stress, *J. Pharm. Sci.*, 2020, **109**, 871–880.

55 J. Homola, Surface Plasmon Resonance Sensors for Detection of Chemical and Biological Species, *Chem. Rev.*, 2008, **108**, 462–493.

56 Z. Zhang, S. Chen and S. Jiang, Dual-Functional Biomimetic Materials: Nonfouling Poly(carboxybetaine) with Active Functional Groups for Protein Immobilization, *Biomacromolecules*, 2006, **7**, 3311–3315.

57 Y. Xia and G. M. Whitesides, Soft Lithography, *Angew. Chem., Int. Ed.*, 1998, **37**, 550–575.

